Supplementary Information

Neuronal activity modifies DNA methylation landscape in the adult brain

Junjie U. Guo[1,2], Dengke K. Ma[1,3], Huan Mo[4], Madeleine P. Ball[5], Mi-Hyeon Jang[1,3], Michael A. Bonaguidi[1,3], Jacob A. Balazer[6], Hugh L. Eaves[4], Bin Xie[7], Eric Ford[8], Kun Zhang[9], Guo-li Ming[1,2,3], Yuan Gao[1,7]* and Hongjun Song[1,2,3]*

[1]Institute for Cell Engineering, [2]The Solomon H. Snyder Department of Neuroscience, [3]Department of Neurology, Johns Hopkins University School of Medicine, Baltimore, Maryland, USA.
[4]Center for the Study of Biological Complexity, Virginia Commonwealth University, Richmond, Virginia, USA.
[5]Department of Genetics, Harvard Medical School, Cambridge, Massachusetts, USA.
[6]Proofpoint Inc., Sunnyvale, California, USA.
[7]Division of Genomics, Epigenomics and Bioinformatics, Lieber Institute for Brain Development, Baltimore, Maryland, USA.
[8]Department of Radiation Oncology, Johns Hopkins University School of Medicine, Baltimore, Maryland, USA.
[9]Department of Bioengineering, University of California at San Diego, La Jolla, California, USA.

Contents:

Supplementary Table 1. MSCC Illumina sequencing statistics.

Sample	Number of reads (total clusters)	Number of reads with appropriate adaptors	Number of mapped reads (percentage)	Number of CpG seen at least once	Average number of reads per CpG
E0-HpaII	24,020,396	17,438,434	12,658,706 (72.6%)	947,711	5.32
E0-Inverse	26,334,571	19,990,984	10,590,651 (53.0%)	1,006,501	4.45
E4-HpaII	37,041,806	28,062,204	21,162,529 (75.4%)	1,051,884	8.89
E4-Inverse	36,840,566	26,105,312	13,036,913 (49.9%)	1,003,625	5.48
E24-HpaII	24,645,278	19,158,832	14,226,530 (78.0%)	997,306	5.98
E24-Inverse	26,161,826	18,235,578	10,000,964 (54.8%)	967,606	4.20

Supplementary Table 2. Primer sets used for bisulfite sequencing analysis of selected CpGs. (Excel file: Table S2)

Supplementary Table 3. Primer sets used for HpaII-qPCR analysis of selected CpGs. (Excel file: Table S3)

Supplementary Table 4. MSCC results for all MSCC30+ sites. (Excel file: Table-S4)

Supplementary Table 5. List of repetitive sequences examined for CpG methylation changes. (Excel file: Table S5)

Supplementary Table 6. Mouse exon array expression profiles of dentate granule cells at E0 and E4. (Excel file: Table S6)

Supplementary Table 7. Expression profiles of genes associated with activity-modified CpGs. (Excel file: Table S7)

Supplementary Table 8. Primer sets and results of q-PCR analysis of promoter CpG changes-associated genes. (Excel file: Table S8)

Supplementary Table 9. Functional pathways that contain activity-modified CpGs. (Excel file: Table S9)

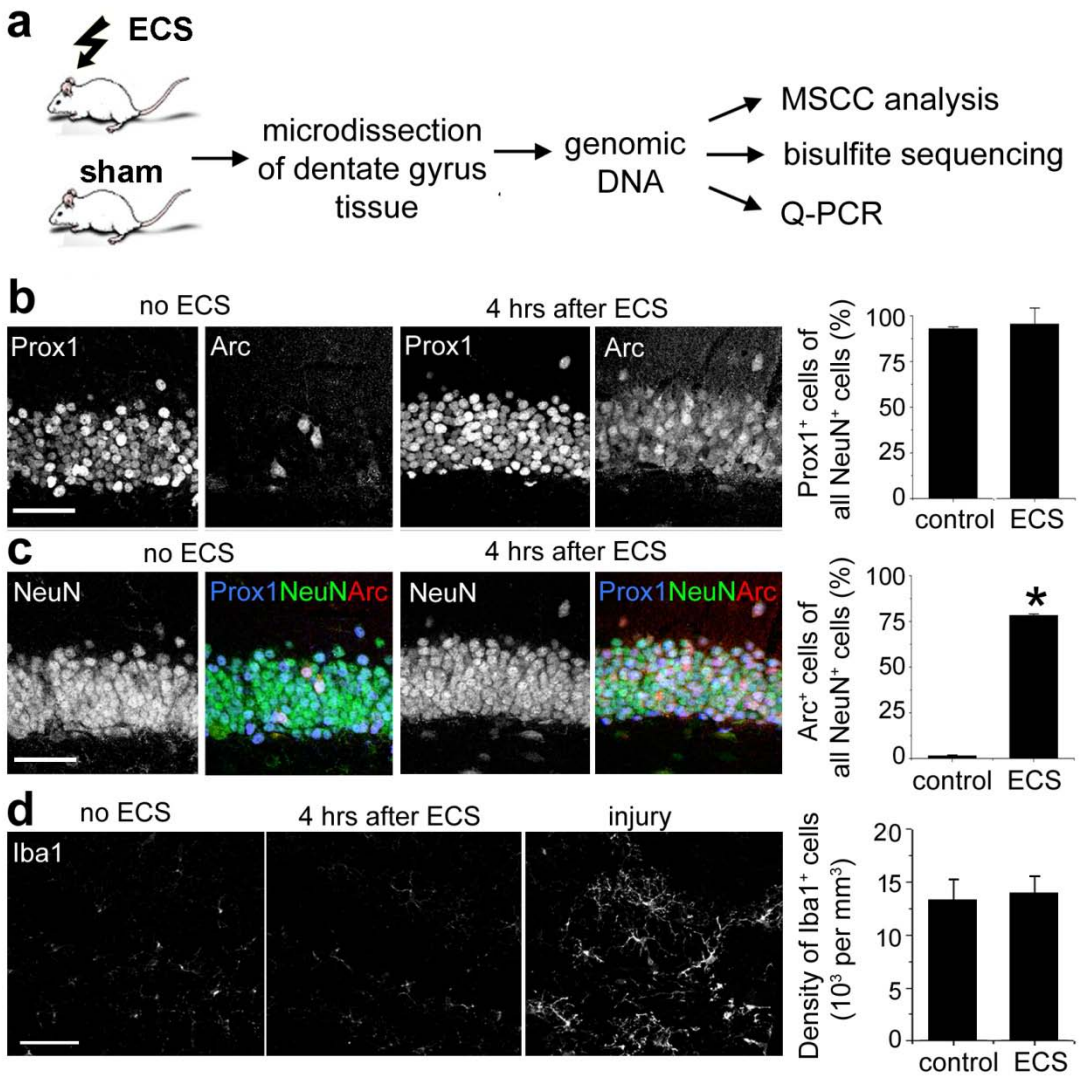

Supplementary Figure 1. Analysis of activity-induced DNA methylation changes in the dentate gyrus of adult mice. (**a**) A schematic diagram of the experimental design. (**b-d**) Synchronous activation of dentate granule neurons in the adult brain by a single ECS**.** Shown are sample confocal images of immunostaining of dentate gyrus for NeuN (mature neuronal marker), Prox1 (dentate granule cell maker), Arc (immediate early gene as a marker for neuronal activation), Iba1 (microglia marker) at 0 or 4 hrs after ECS. Scale bar: 50 μm. Also shown are quantifications of percentages of $Prox1^+NeuN^+$ cells, Arc^+NeuN^+ cells among all $NeuN^+$ cells, and stereological counting of $Iba1^+$ cells in the adult dentate gyrus. Values represent mean ± s.e.m. (n = 3). Note that ~ 90% of $NeuN^+$ neurons in the adult dentate gyrus are $Prox1^+$ dentate granule cells (**b**). ECS is very effective in activating $NeuN^+$ neurons *in vivo* (**c**). In addition, ECS does not change the number of $Iba1^+$ microglia cells in the adult dentate gyrus (**d**), nor leads to activation of microglia cells, which exhibit different morphology (such as after injury).

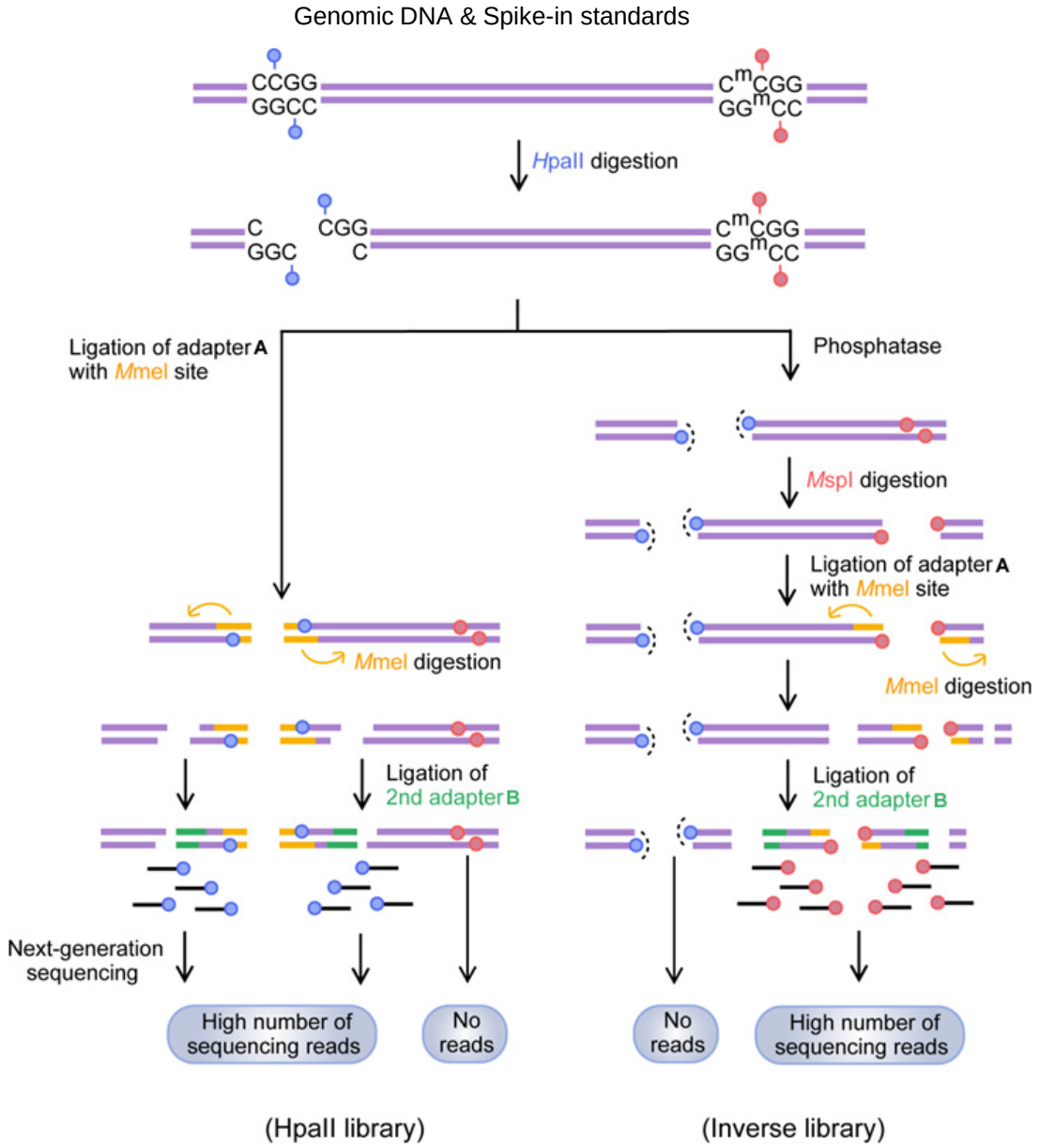

Supplementary Figure 2. A schematic diagram of the MSCC method for nonbiased digital profiling of the methylation status at the single nucleotide resolution across the whole genome. Methyl-sensitive Cut Counting (MSCC) profiles CpG methylation levels across the whole genome by using two restriction enzymes, the methylation-sensitive HpaII and its methylation-insensitive isoschizomer MspI. Both enzymes recognize CCGG sequences. HpaII cuts unmethylated CCGG sites, but not methylated or hydroxymethylated ones[48], whereas MspI cuts all CCGG sites. Sequencing read counts matched to HpaII and MspI cutting sites provide a quantitative and digital measurement of CpG methylation levels within the CCGG sites. Detailed description of the original MSCC method can be found in ref[7].

a

	All CpG sites	All CCGG sites	MSCC sites (30+ reads)
Total	21,342,779	1,594,148	219,991
% of All CpGs	100%	7.50%	1.03%

b

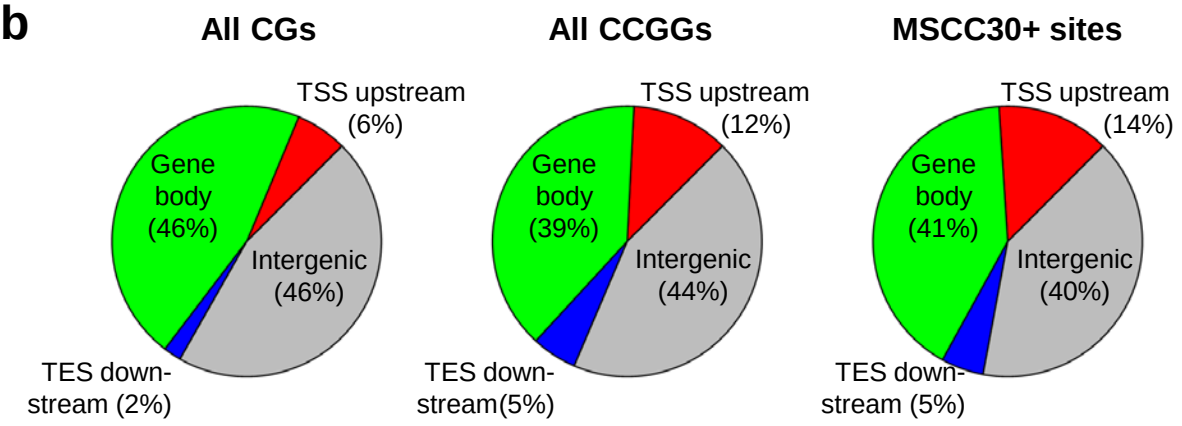

c

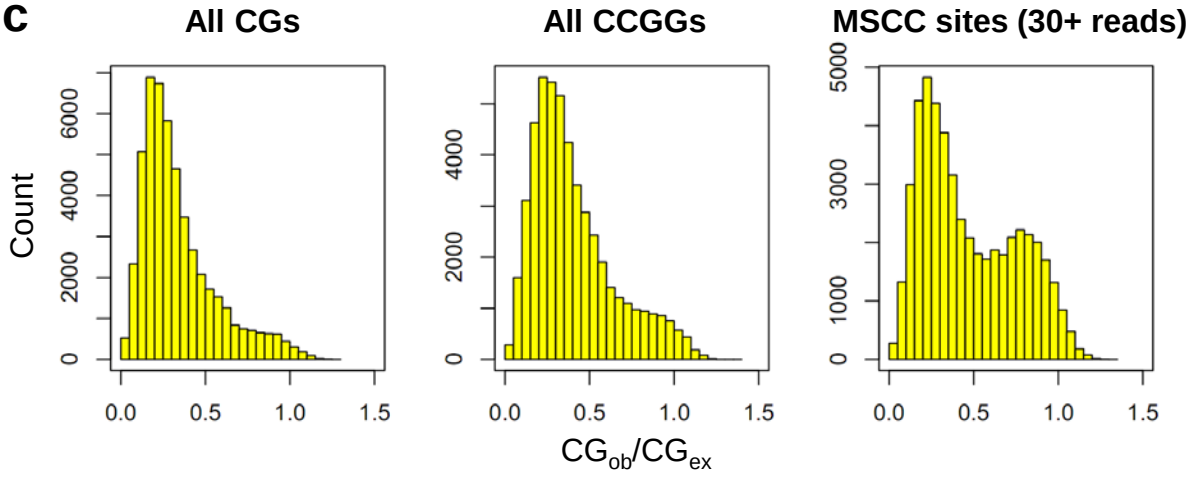

Supplementary Figure 3. Genomic distribution of MSCC-profiled CpGs. (**a**) A table of the number of all CG dinucleotides in the mouse genome, all CCGG sequences (MSCC site), and MSCC sites with at least 30 reads, and their percentage in all CpGs. (**b**) Percentile distribution of subsets of CpGs within different genomic subregions. TSS: transcription start site; Gene body: exons and introns; Intergenic: over 5 kb away from any known genes; TSS upstream: 5 kb upstream from the TSS; TES downstream: 5 kb downstream from the transcription end site (TES). (**c**) Distribution of local CG densities of different subsets of CpGs. Shown are histograms of counts along the ratio of observed (CG_{ob}) over expected CG (CG_{ex}) numbers. A total of 50,000 random sites in the mouse genome from each subset were analysed in (**b, c**).

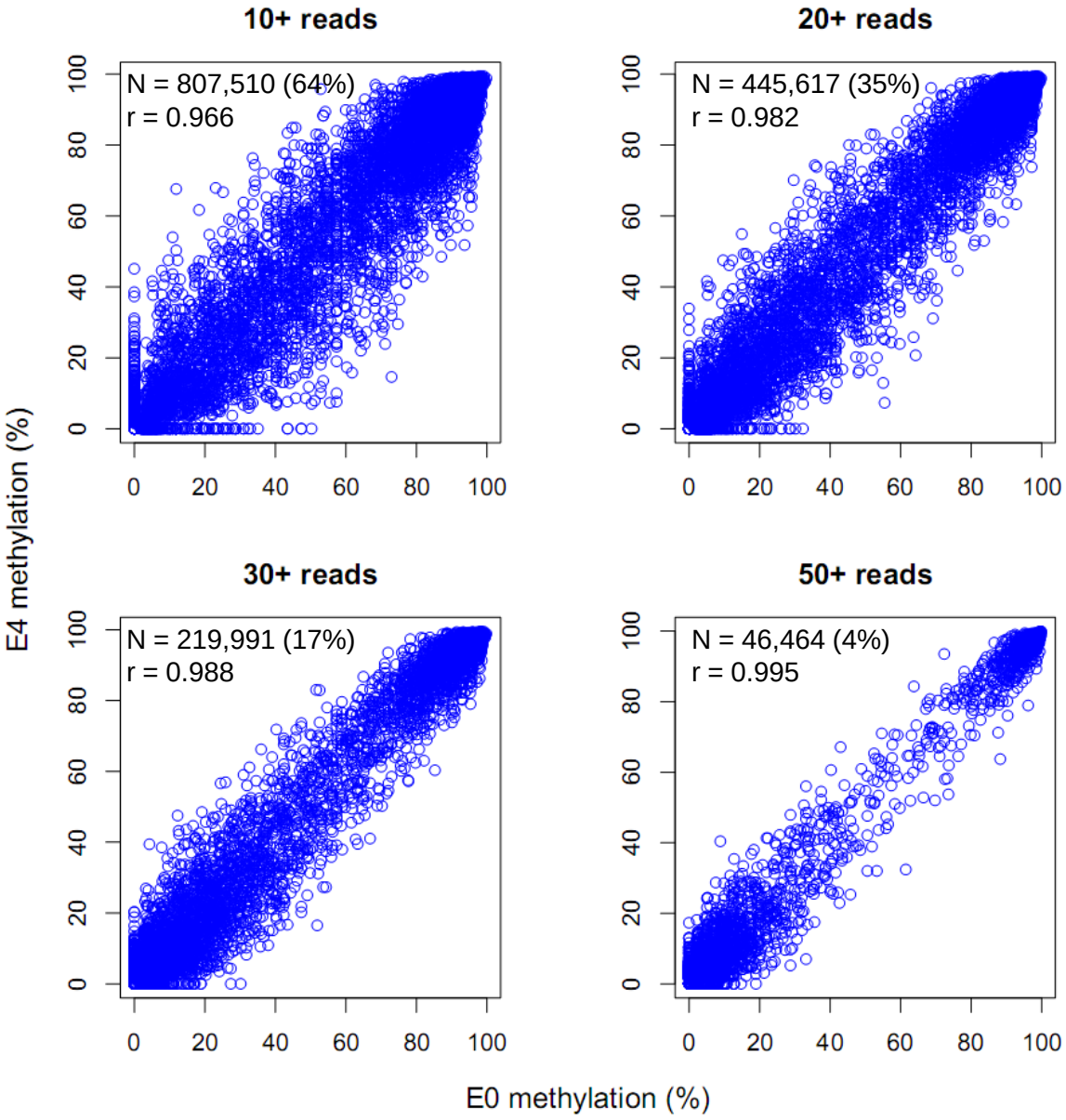

Supplementary Figure 4. Effect of MSCC sequencing depth on the accuracy of methylation estimates. Pair-wise comparison was performed on E0 and E4 methylation levels of 4 subsets of MSCC sites using different depth filters (10+ reads; 20+ reads; 30+ reads; 50+ reads). Also shown are total numbers of CpGs measured, their percentages in all MSCC sites (1,262,730 sites at least one read), and Pearson's correlations (r).

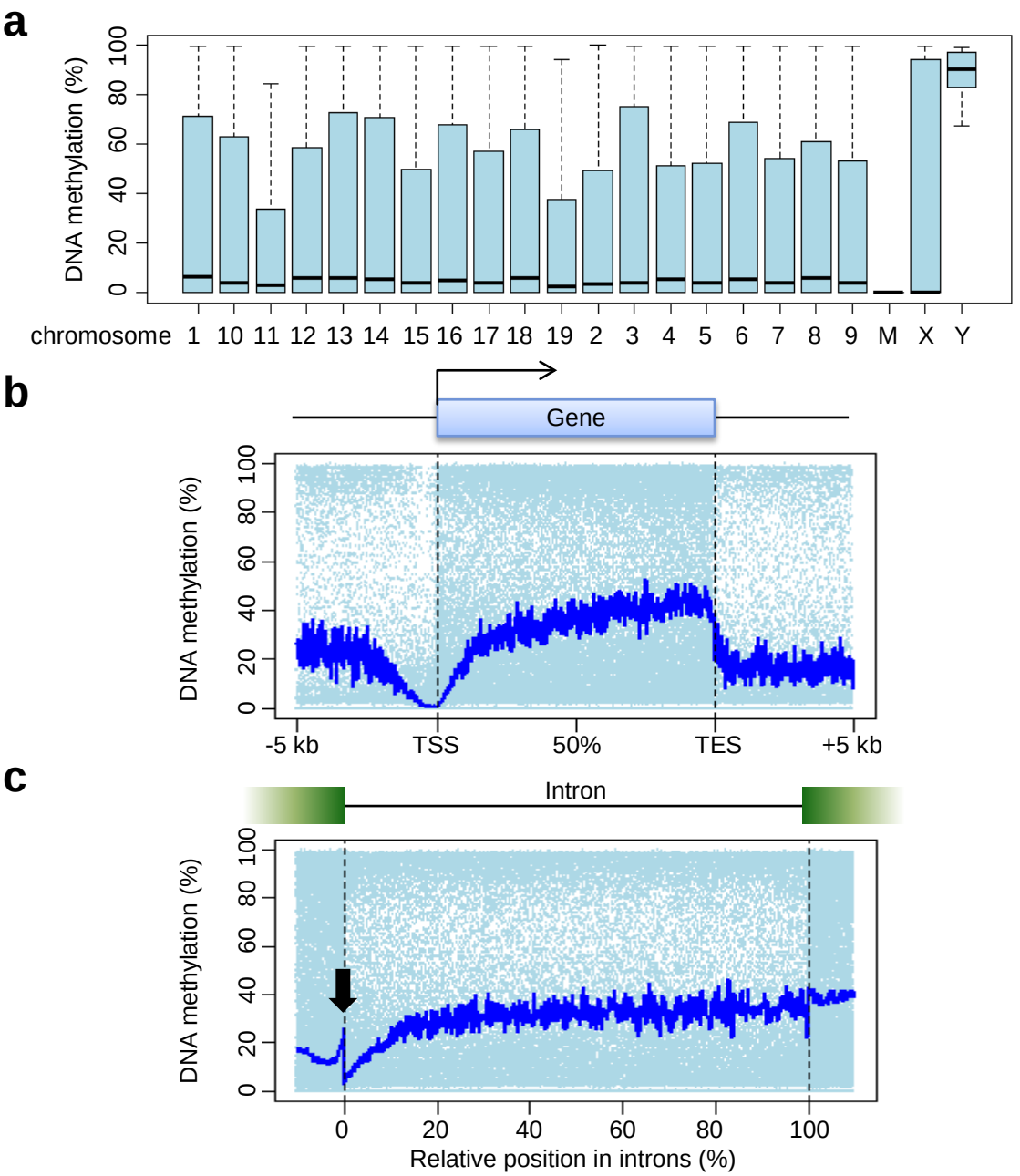

Supplementary Figure 5. Global properties of CpG methylation in mouse hippocampal granule neurons. (**a**) Overall methylation levels of each chromosome. Note that the mitochondrial genome (M) is almost completely unmethylated, whereas the Y chromosome is hypermethylated. (**b**) Individual CpG methylation levels are mapped to their relative location to nearby genes (cyan dots). The blue line shows the moving average. (**c**) Individual CpG methylation levels are mapped to their relative location to nearby splicing sites (cyan dots). The blue line shows the moving average. As previously reported (ref[34]), there is a sharp spike in methylation level at exon-intron junctions (black arrow), followed by a gradual increase in methylation levels within introns.

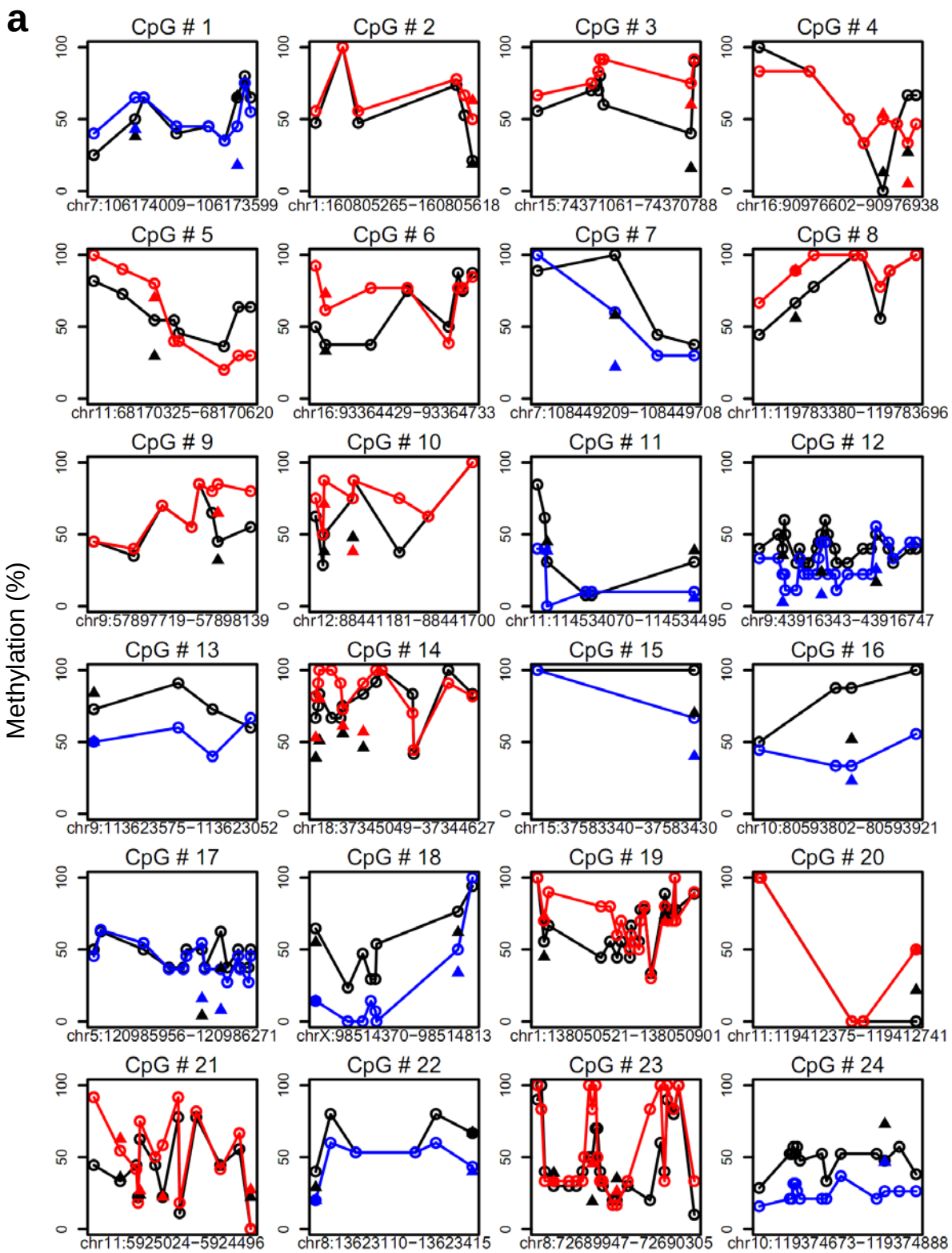
a
Methylation (%)
CpG # 1
chr7:106174009-106173599
CpG # 2
chr1:160805265-160805618
CpG # 3
chr15:74371061-74370788
CpG # 4
chr16:90976602-90976938
CpG # 5
chr11:68170325-68170620
CpG # 6
chr16:93364429-93364733
CpG # 7
chr7:108449209-108449708
CpG # 8
chr11:119783380-119783696
CpG # 9
chr9:57897719-57898139
CpG # 10
chr12:88441181-88441700
CpG # 11
chr11:114534070-114534495
CpG # 12
chr9:43916343-43916747
CpG # 13
chr9:113623575-113623052
CpG # 14
chr18:37345049-37344627
CpG # 15
chr15:37583340-37583430
CpG # 16
chr10:80593802-80593921
CpG # 17
chr5:120985956-120986271
CpG # 18
chrX:98514370-98514813
CpG # 19
chr1:138050521-138050901
CpG # 20
chr11:119412375-119412741
CpG # 21
chr11:5925024-5924496
CpG # 22
chr8:13623110-13623415
CpG # 23
chr8:72689947-72690305
CpG # 24
chr10:119374673-119374888

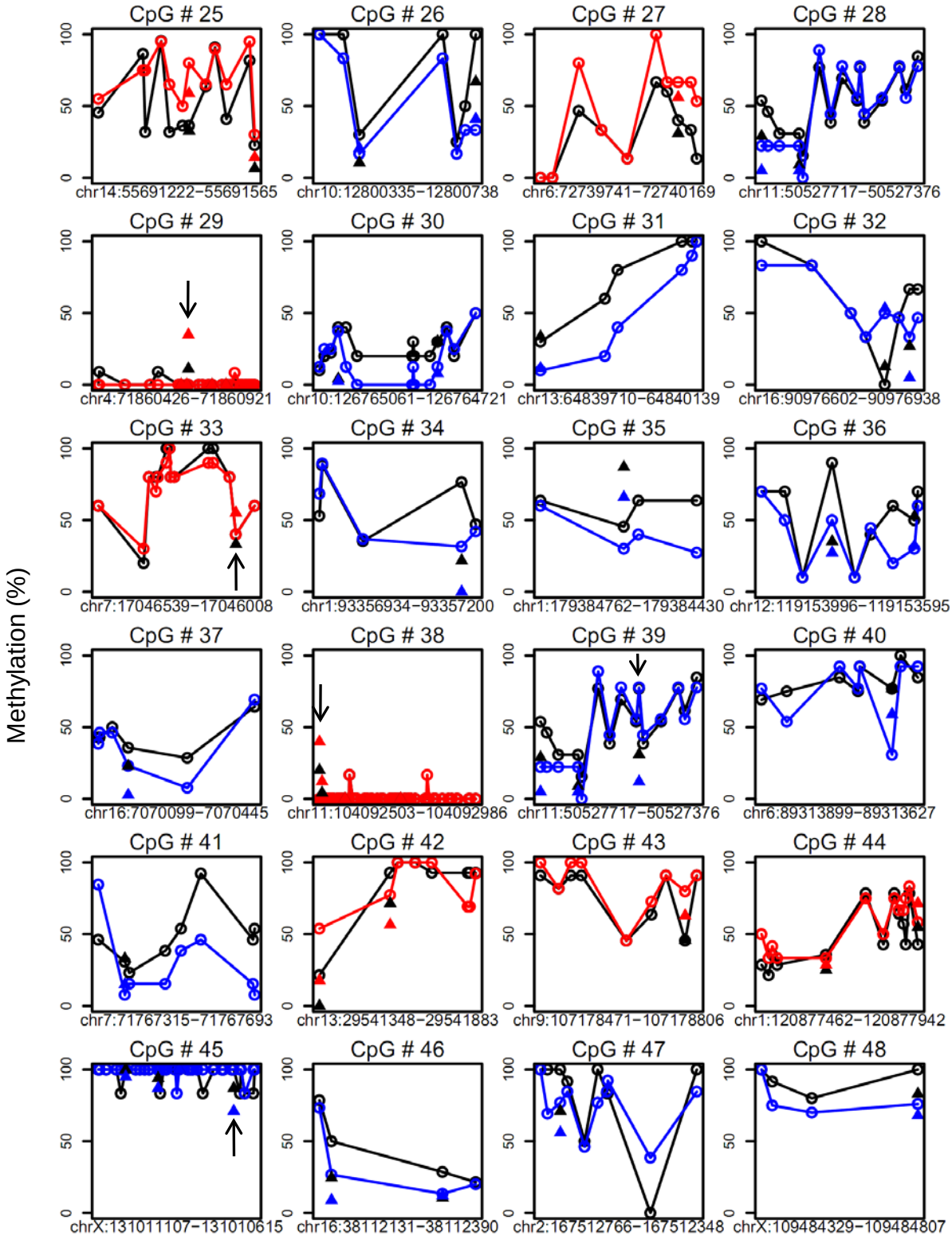
Methylation (%)
CpG # 25
chr14:55691222-55691565
CpG # 26
chr10:12800335-12800738
CpG # 27
chr6:72739741-72740169
CpG # 28
chr11:50527717-50527376
CpG # 29
chr4:71860426-71860921
CpG # 30
chr10:126765061-126764721
CpG # 31
chr13:64839710-64840139
CpG # 32
chr16:90976602-90976938
CpG # 33
chr7:17046539-17046008
CpG # 34
chr1:93356934-93357200
CpG # 35
chr1:179384762-179384430
CpG # 36
chr12:119153996-119153595
CpG # 37
chr16:7070099-7070445
CpG # 38
chr11:104092503-104092986
CpG # 39
chr11:50527717-50527376
CpG # 40
chr6:89313899-89313627
CpG # 41
chr7:71767315-71767693
CpG # 42
chr13:29541348-29541883
CpG # 43
chr9:107178471-107178806
CpG # 44
chr1:120877462-120877942
CpG # 45
chrX:131011107-131010615
CpG # 46
chr16:38112131-38112390
CpG # 47
chr2:167512766-167512348
CpG # 48
chrX:109484329-109484807
0
50
100

b

MSCC cut-off (%)	# CpGs	Validated	Specificity (%)	Sensitivity (%)
± 40	25	6/6	100	13.0
± 30	294	16/16	100	32.6
± 25	1011	28/28	100	58.7
± 20	3050	35/37	94.6	76.1
± 15	8190	43/48	89.6	93.5

c

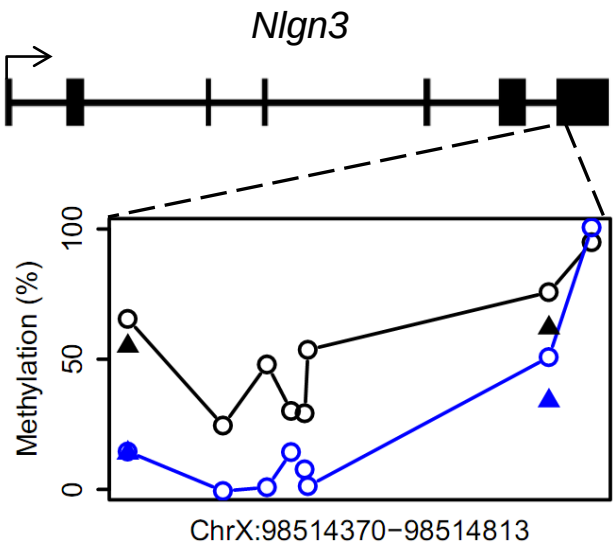

Supplementary Figure 6. Bisulfite sequencing validation of DNA methylation changes of selected CpGs identified by the MSCC method. (**a**) Supporting data for **Fig. 1b.** Shown are summaries of bisulfite sequencing analysis of 48 selected regions with MSCC-detected methylation changes ($\Delta_{MSCC,\ E4\text{-}E0} \geq 15\%$). Lines show bisulfite sequencing results (black: E0; red: E4 *de novo* methylated; blue: E4 demethylated). Corresponding MSCC estimates are shown by triangles. Independent biological samples were used for MSCC analysis and bisulfite sequencing analysis. Values represent mean from ≥ 20 bisulfite sequencing reads for each condition from at least two animals. Arrows point to false positive sites. (**b**) A summary table of specificity and sensitivity of MSCC method to detect differential methylation levels (See formulas used for calculation in *Methods*). (**c**) Activity-induced demethylation of CpGs within the gene body of *Nlgn3* as shown by bisulfite sequencing analysis. The demethylation of two CpGs indicated from the MSCC analysis with relatively low sequencing depth (< 30 reads) was validated by bisulfite sequencing analysis.

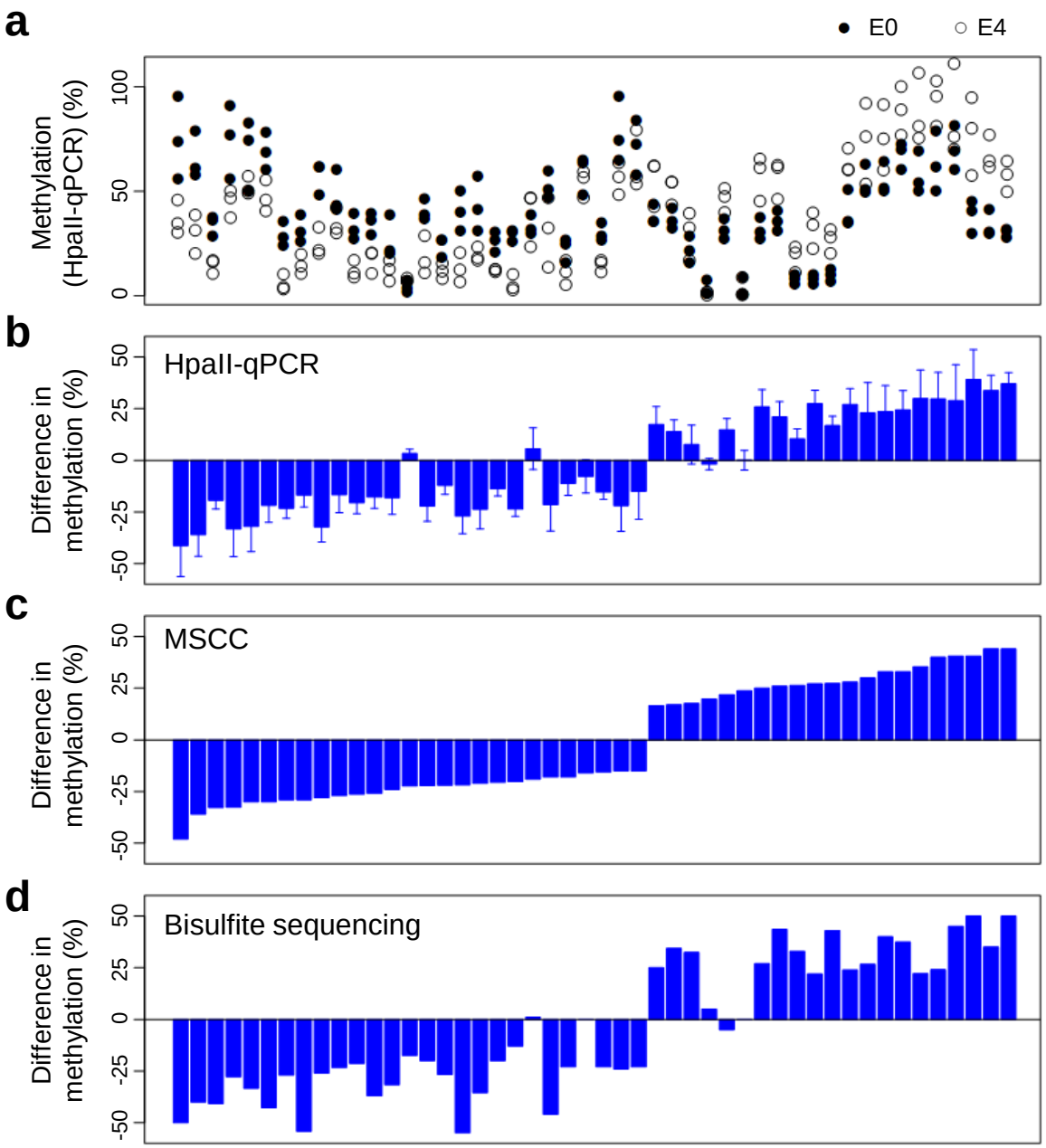

Supplementary Figure 7. Methylation sensitive q-PCR analysis of variability and reproducibility of methylation changes detected by MSCC method. An HpaII-based methylation-sensitive q-PCR method was used to quantify the level of DNA methylation at specific CpGs from multiple animals at E0 and at E4. (**a**) Strip plots of methylation levels of 48 CpGs of individual animals at E0 (filled circles) and E4 (open circles). (**b**) Mean methylation differences based on HpaII-qPCR. Values represent mean ± s.d. (n = 3 animals). (**c, d**) Differences in methylation of the same CpGs as measured by MSCC and bisulfite sequencing (same data set as in **Fig. 1b** and **Supplementary Fig. 6a**).

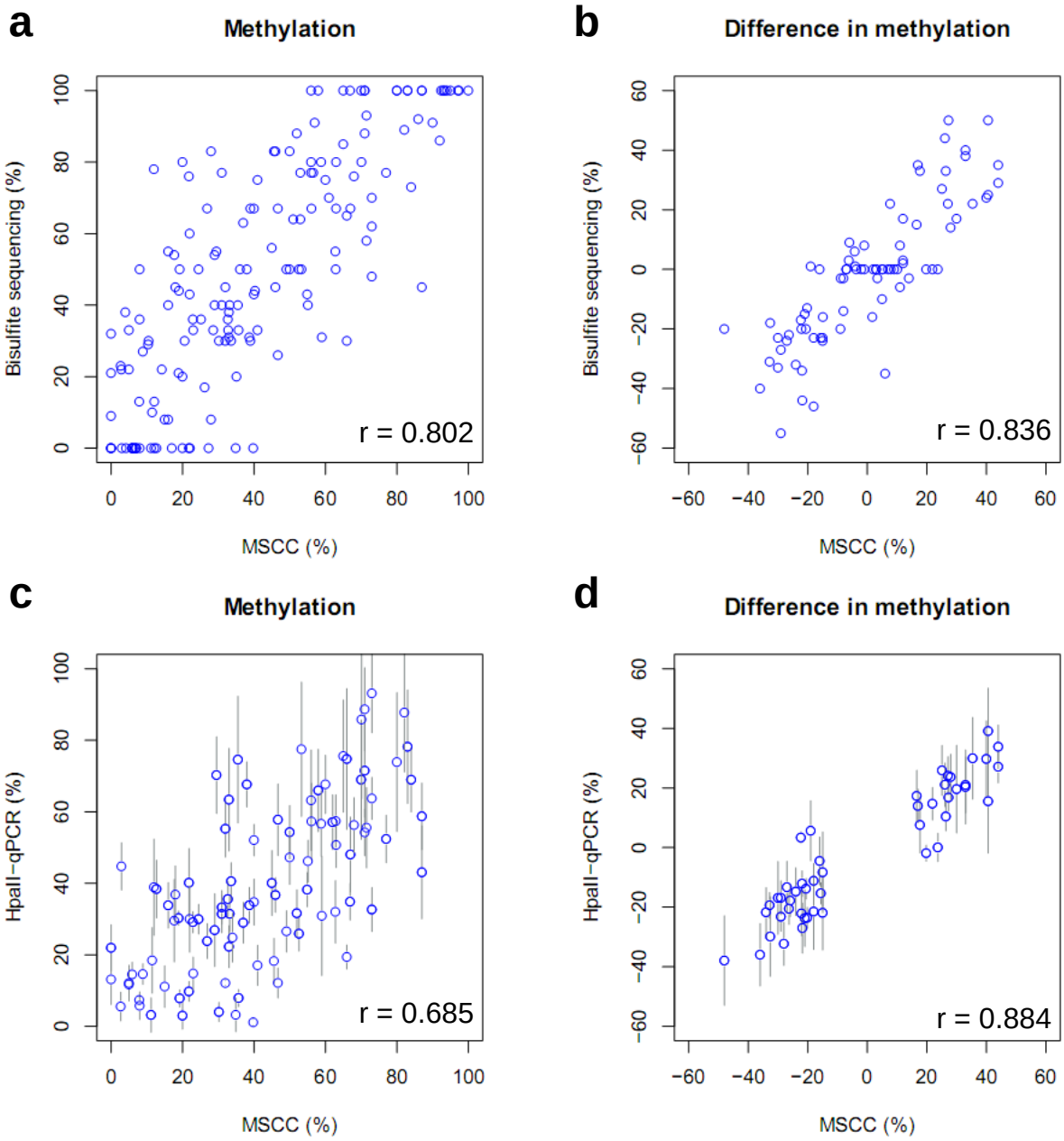

Supplementary Figure 8. Correlation between MSCC method and bisulfite sequencing analysis and between MSCC method and HpaII-qPCR analysis on methylation levels and differential methylation estimates. Bisulfite sequencing results of all selected CpGs at E0 and E4 (**a**), and differential methylation calculated from these results (**b**) are plotted against MSCC estimates. Similarly, HpaII-based methylation sensitive q-PCR analysis of selected CpGs (same as in **Supplementary Fig. 6**) from three individual animals at E0 and E4 each (**c**) and differential methylation calculated from these results (**d**) are plotted against MSCC estimates. Values represent mean ± s.d. (n = 3). Pearson's correlation (r) is shown.

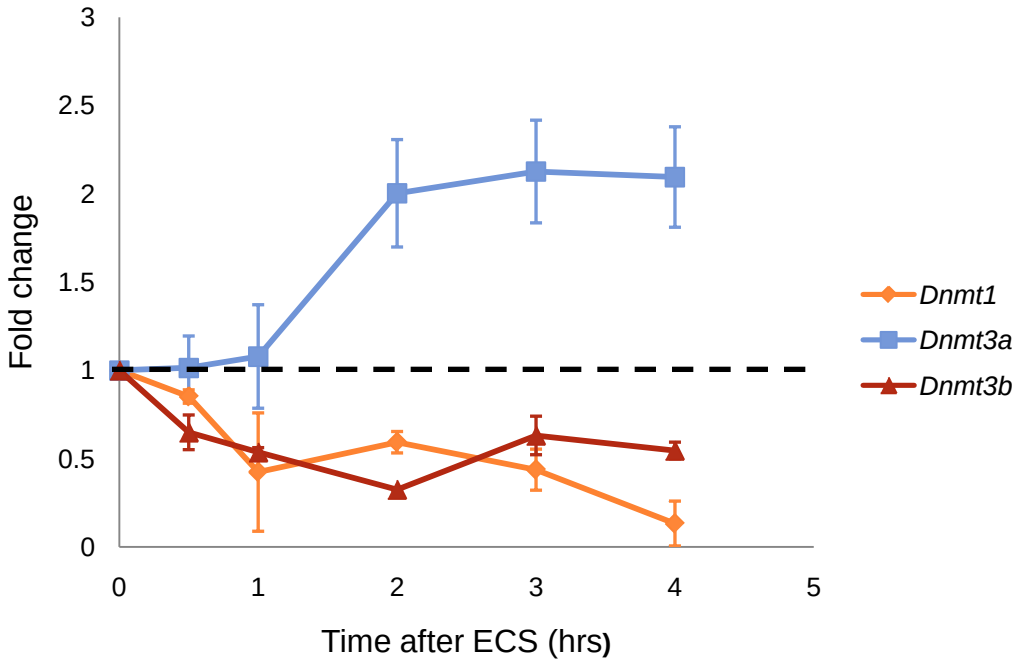

* *Dnmt3l* was undetectable

Supplementary Figure 9. Time course on the expression of DNA methyltransferases (DNMTs) in the dentate gyrus of the adult mouse hippocampus before and after a single ECS. Values represent mean ± s.d. from q-PCR analysis (n = 3).

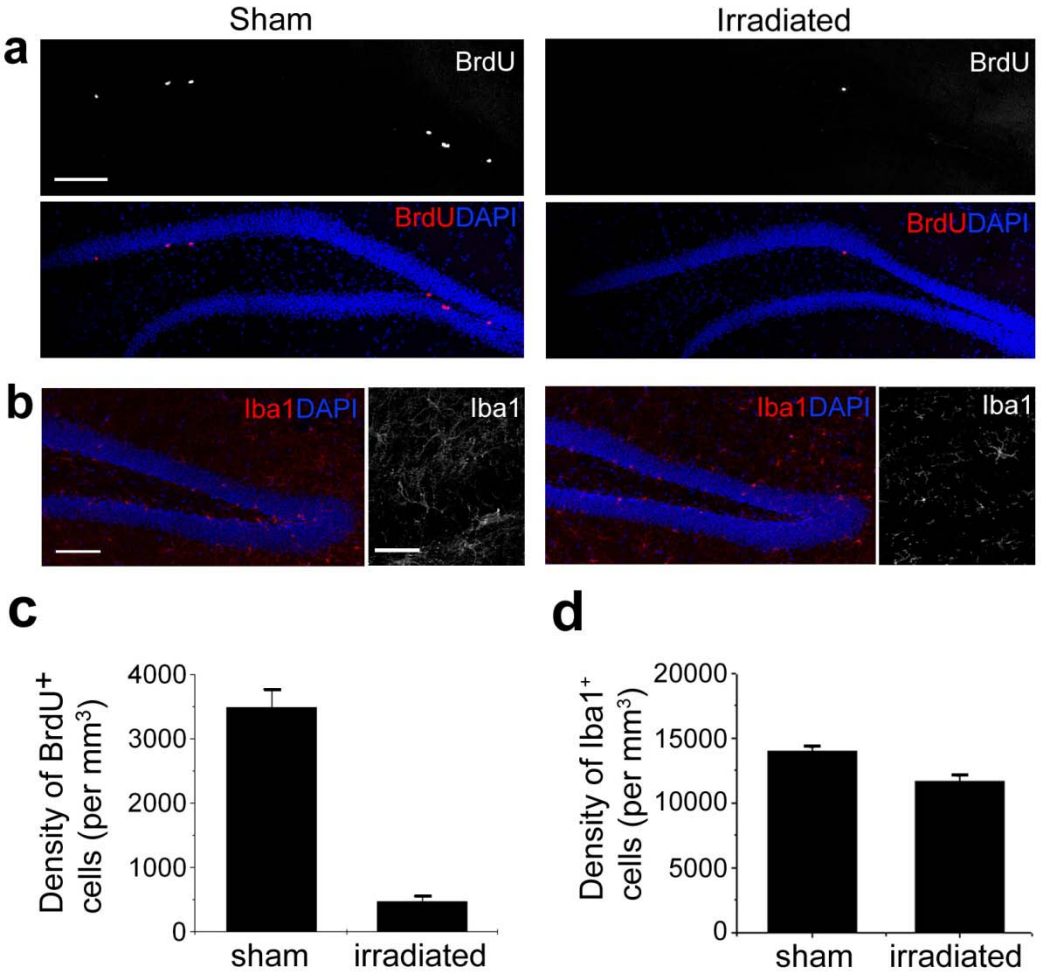

Supplementary Figure 10. Inhibition of cell proliferation in the dentate gyrus of adult mouse hippocampus after local irradiation. Adult male mice received targeted irradiation at hippocampal regions. At 5 weeks after irradiation they were pulsed with BrdU (200 mg/kg body weight, *i.p.*), followed by fixation 2 hrs later. Shown are sample confocal images of DAPI staining and immunostaining for BrdU (**a**) or microglia marker Iba1 (**b**) of dentate gyrus in animals with irradiation and sham control. Also shown are summaries of stereological counting of $BrdU^+$ cells (**c**) or $Iba1^+$ cells (**d**) within the dentate gyrus. Note the dramatic reduction of dividing cells, but no change in number of $Iba1^+$ microglia cells at five weeks after irradiation when methylation analysis was carried out. Scale bars: 100 μm (**a**) and 50 μm (**b**).

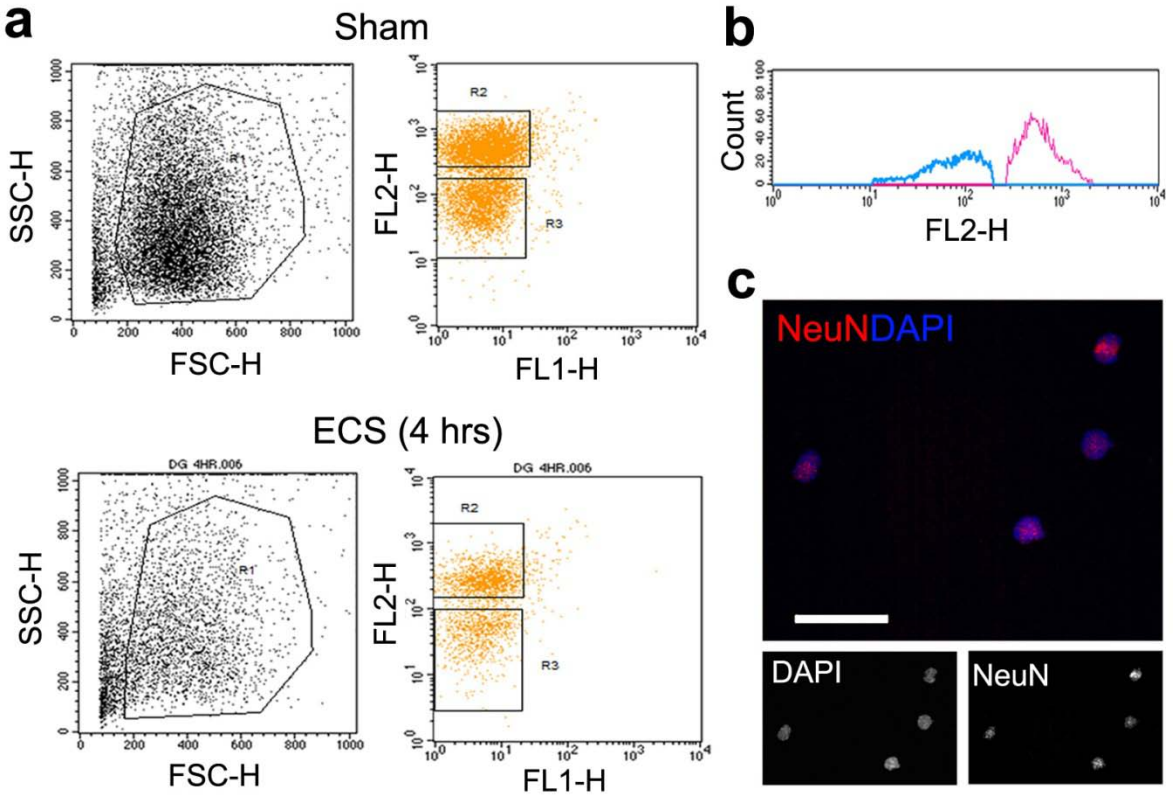

Supplementary Figure 11. Purification of NeuN$^+$ mature neuronal nuclei from the dentate gyrus of the adult mouse hippocampus by fluorescence activated cell sorting (FACS). Adult mice were administered ECS or sham treatment, and the dentate gyrus tissue was removed 4 hrs later. Nuclei were isolated and processed for immunostaining with the mature neuronal marker NeuN and conjugated R-PE. (**a**) Singular nuclei (R1) were separated from cell debris according to forward scatter (FSC) and side scatter (SSC) profiles for sham and ECS treated samples. The NeuN$^+$ fraction (R2) was separated according to PE levels above the negative isotype control (R3, NeuN$^-$) in sham and ECS conditions. (**b**) Sorting profile demonstrated that the FACS gates had no overlap. (**c**) Immunofluorescence image of post-sorted samples confirmed pure NeuN$^+$ nuclei population. Scale bar: 20 μm.

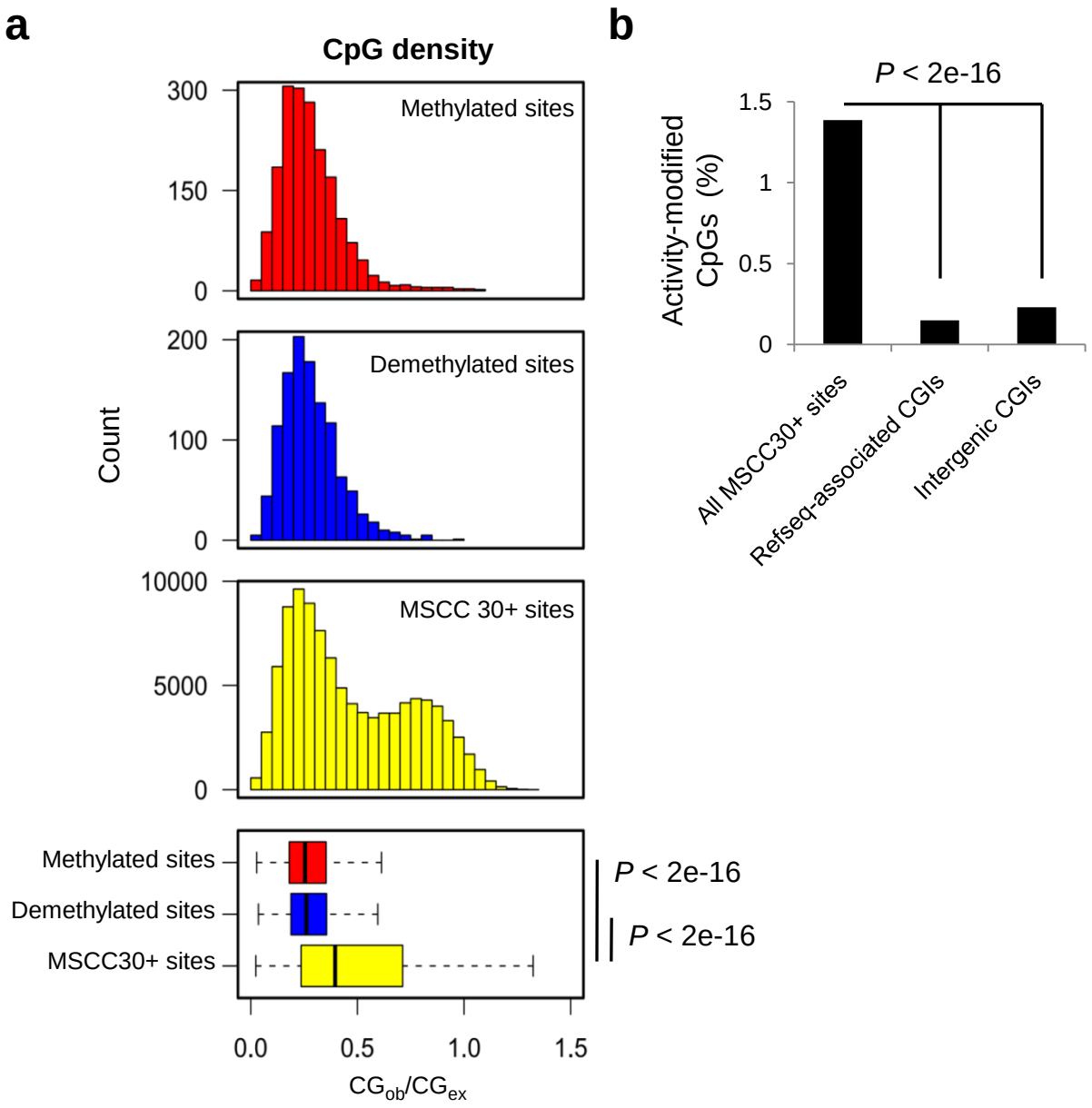

Supplementary Figure 12. CpGs within the low CpG density context as main targets for activity-induced demethylation and *de novo* methylation in mature neurons in the adult brain. (**a**) CpGs that are *de novo* methylated (red) or demethylated (blue) are binned by their CpG densities of 500 bp flanking regions ($\Delta_{MSCC,\ E4\text{-}E0} \geq 20\%$), and compared to all MSCC30+ sites (random 50,000 sites were analysed). Box-plots show medians and quartiles of these 3 distributions (*P* values, Student's t-test). (**b**) Both gene-associated and intergenic CpG islands (CGIs; experimentally determined by Illingworth et al. ref[38]) are resistant to activity-induced methylation changes. Shown are percentages of MSCC30+ sites mapped within two types of CGIs that were modified (≥20%) by ECS, compared to all MSCC30+ sites (*P* value, chi-square test).

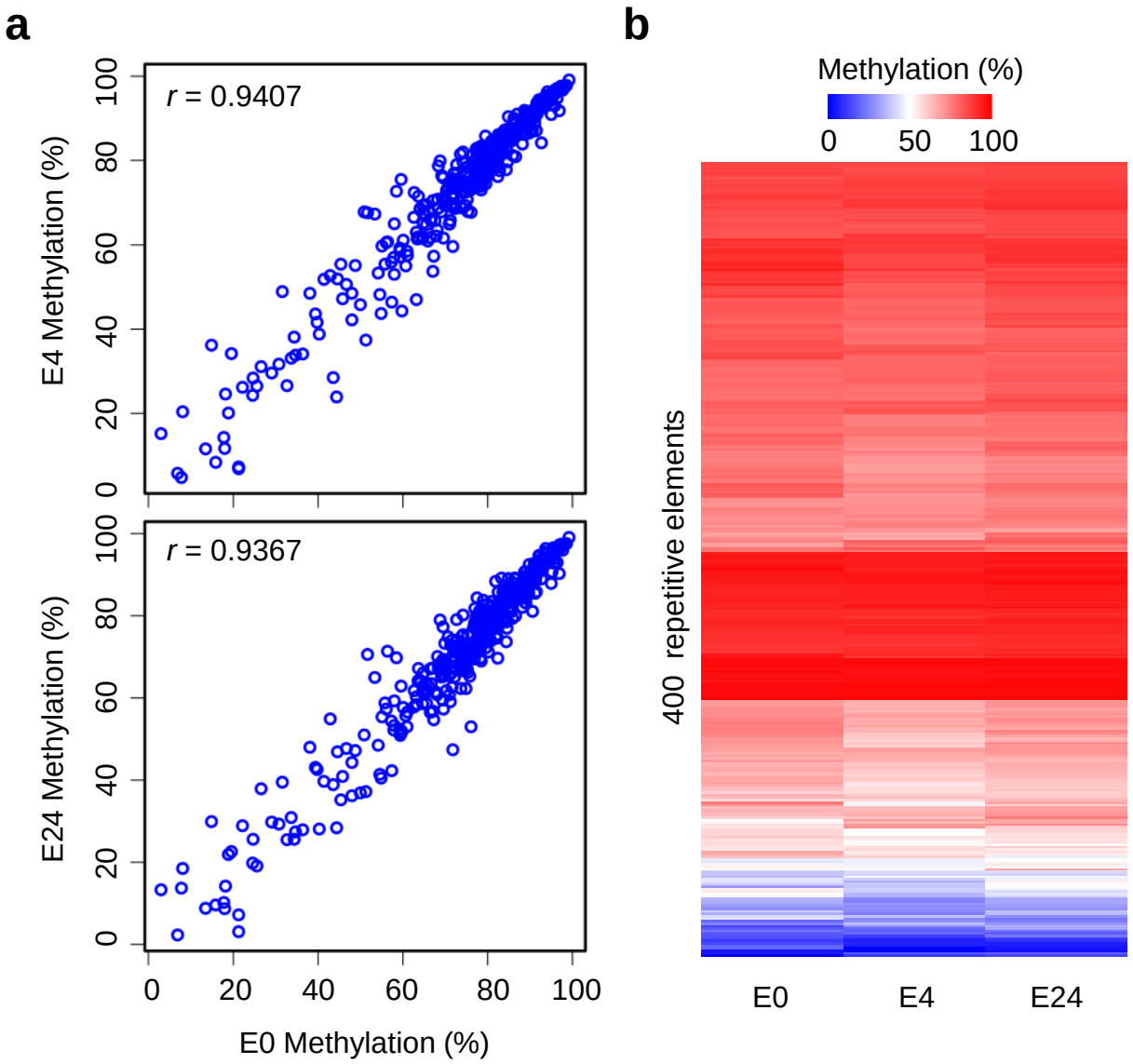

Supplementary Figure 13. Lack of activity-induced methylation changes for CpGs within repetitive sequences in mature neurons in the adult brain. (**a**) Scatter plots show pair-wise comparisons of methylation profiles of 400 repetitive elements at E0, E4, and E24. Pearson's *r* is shown. (**b**) Unsupervised clustering analysis shows highly similar patterns of repetitive element methylation levels at all time points. Note that most repetitive elements are heavily methylated.

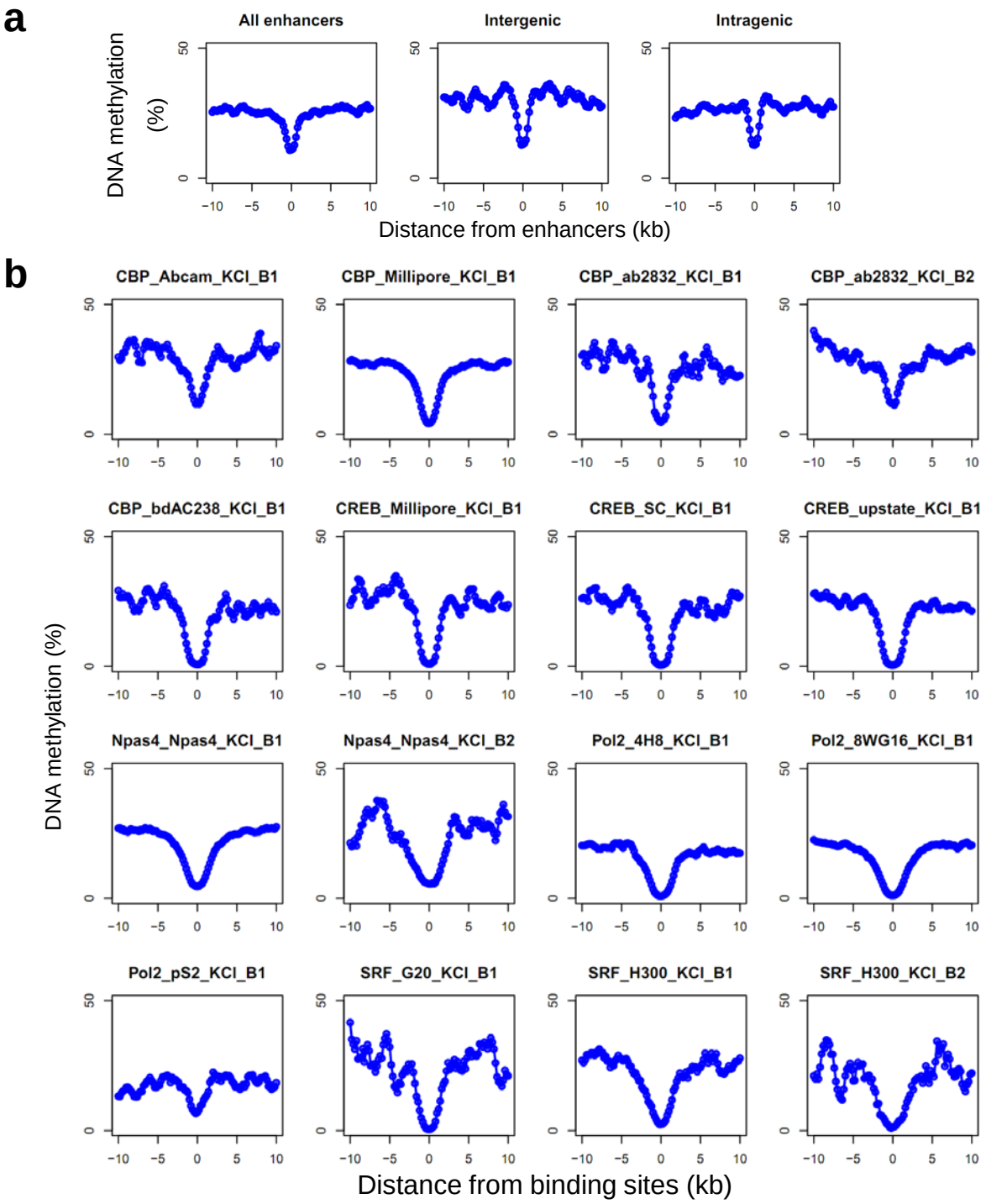

Supplementary Figure 14. Hypomethylation of neuronal activity-dependent enhancers and transcription factor binding sites. (**a**) Both intergenic and intragenic neuronal enhancers are hypomethylated in dentate granule neurons. (**b**) All activity-regulated transcription factor binding sites are hypomethylated in dentate granule neurons. All binding sites were profiled and neuronal enhancers were defined in Kim et al. ref[41].

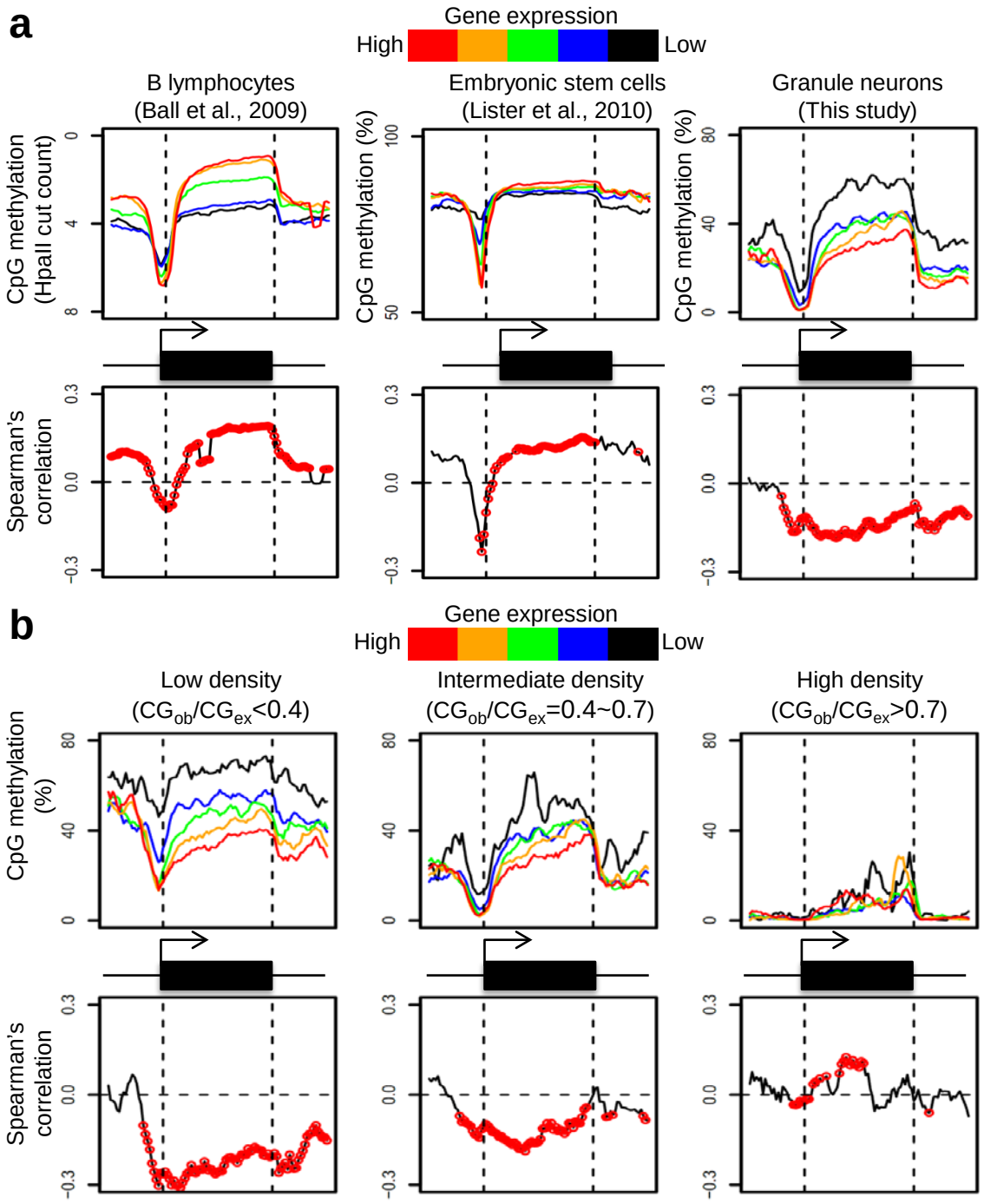

Supplementary Figure 15. Relationship between CpG methylation and gene expression. (**a**) Correlation between CpG methylation and gene expression in dentate granule neurons was compared to MSCC-profiled B lymphocytes[7] and MethylC-seq-profiled H1 embryonic stem cells[34]. Averaged methylation levels for genes expressed at different levels were shown (top). Also shown are Spearman's correlation coefficients (bottom). Dashed lines indicate TSS and TES positions. Red circles indicate observations of *P* values < 0.01. (**b**) Correlation between CpG methylation at different densities and gene expression in dentate granule neurons.

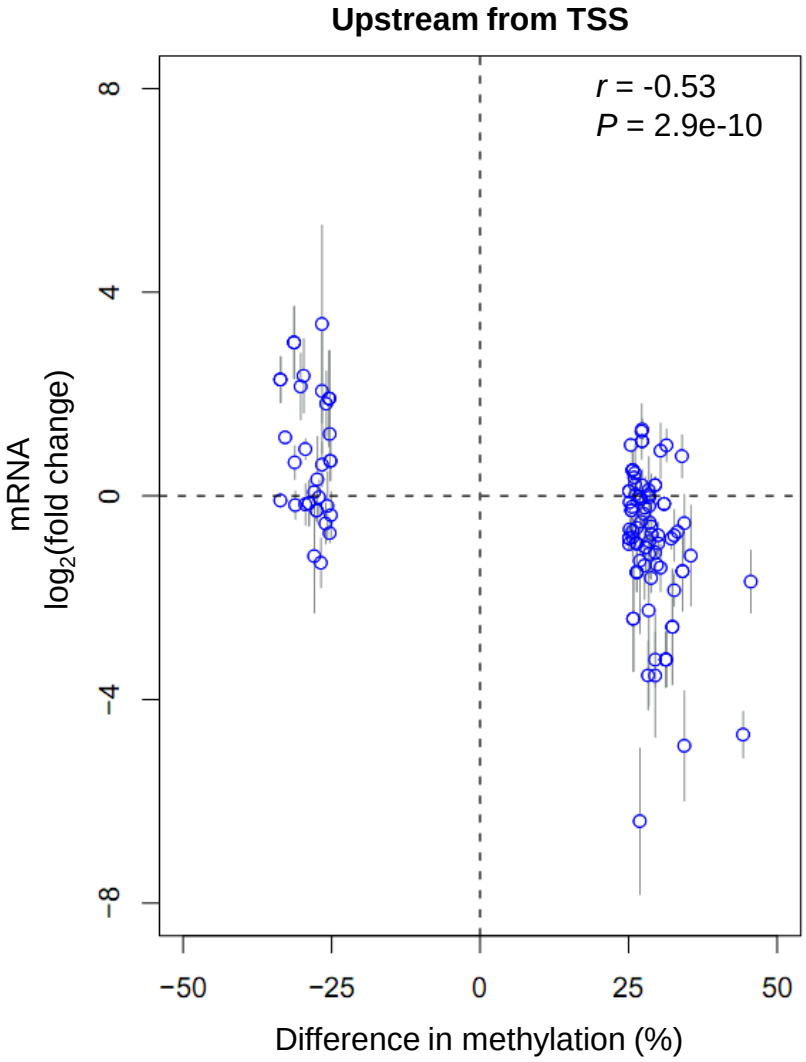

Supplementary Figure 16. Anti-correlation between methylation changes in TSS upstream regions and expression changes of associated genes. Shown is a plot of expression analysis of genes that exhibited methylation changes within 5 kb upstream from TSS ($\Delta_{MSCC} \geq 25\%$; the same set as in **Fig. 6a** left) by q-PCR from 3 independent sets of experiments. Values represent mean $\pm$ s.d. (n = 3).

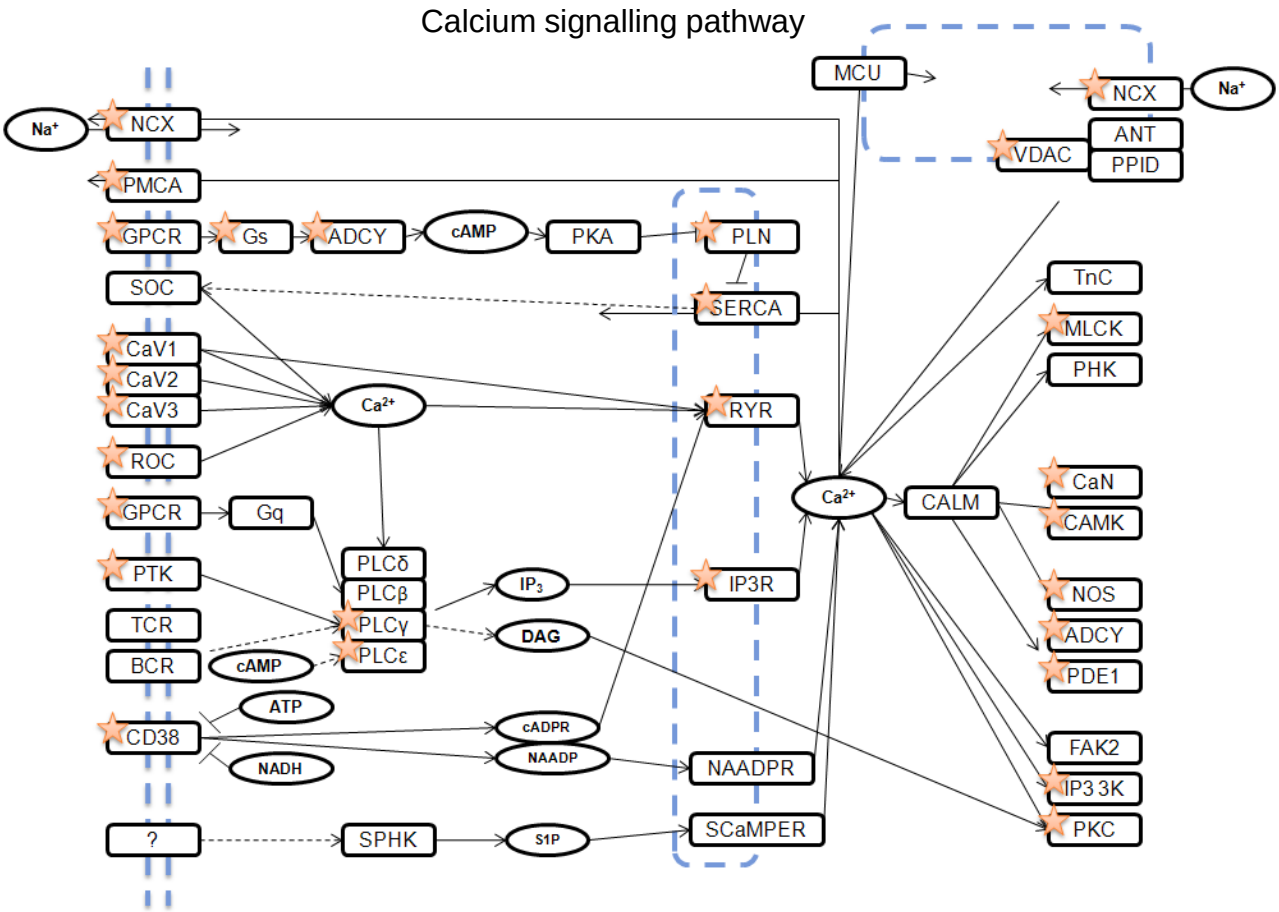

Supplementary Figure 17. Activity-induced methylation changes in genes associated with Ca^{2+} signalling pathway. Pathway diagrams are modified from Kyoto Encyclopedia of Genes and Genomes (KEGG). Genes that harbour activity-induced CpG methylation changes are indicated by stars.

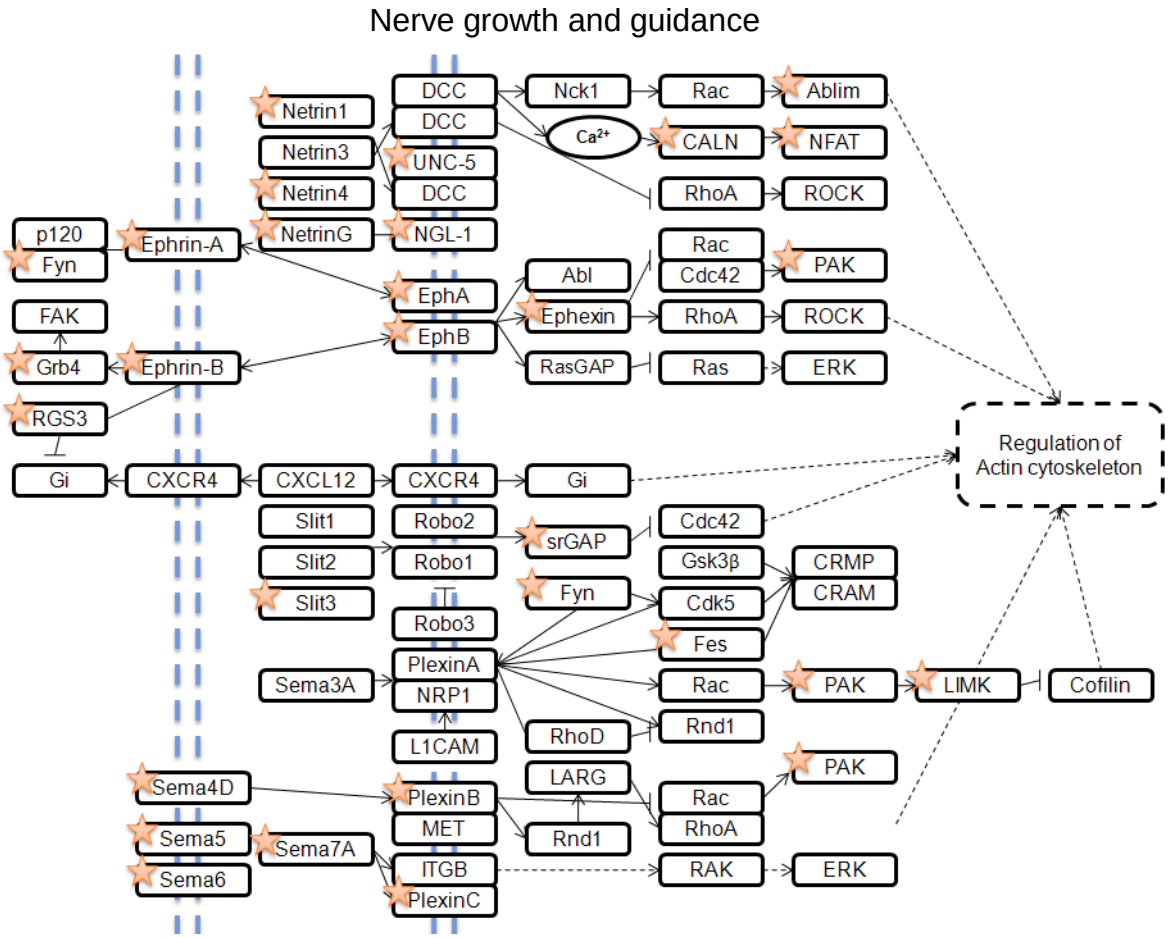

Supplementary Figure 18. Activity-induced methylation changes in genes associated with nerve growth and guidance pathway. Pathway diagrams are modified from Kyoto Encyclopedia of Genes and Genomes (KEGG). Genes that harbour activity-induced CpG methylation changes are indicated by stars.

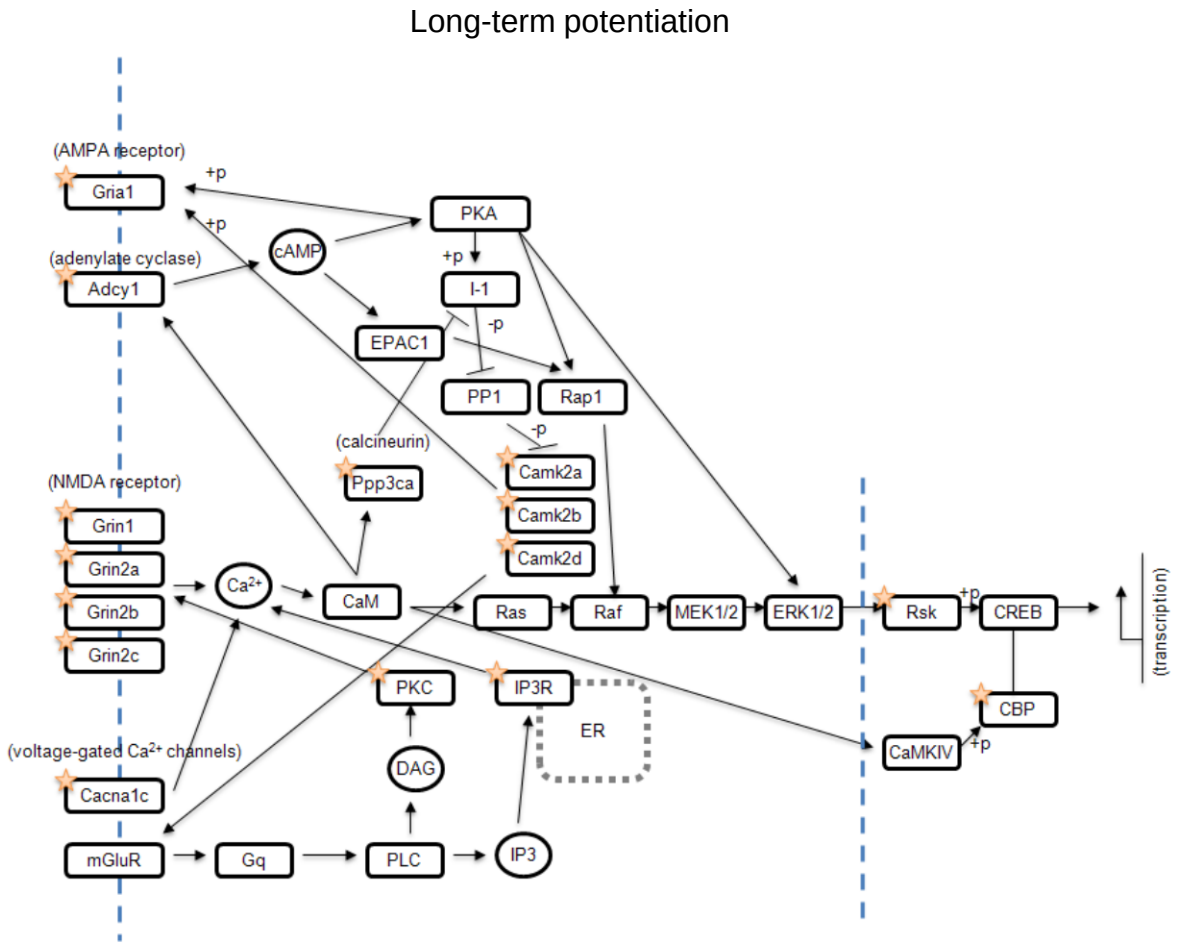

Supplementary Figure 19. Activity-induced methylation changes in genes associated with long-term potentiation pathways. Pathway diagrams are modified from Kyoto Encyclopedia of Genes and Genomes (KEGG). Genes that harbour activity-induced CpG methylation changes are indicated by stars.

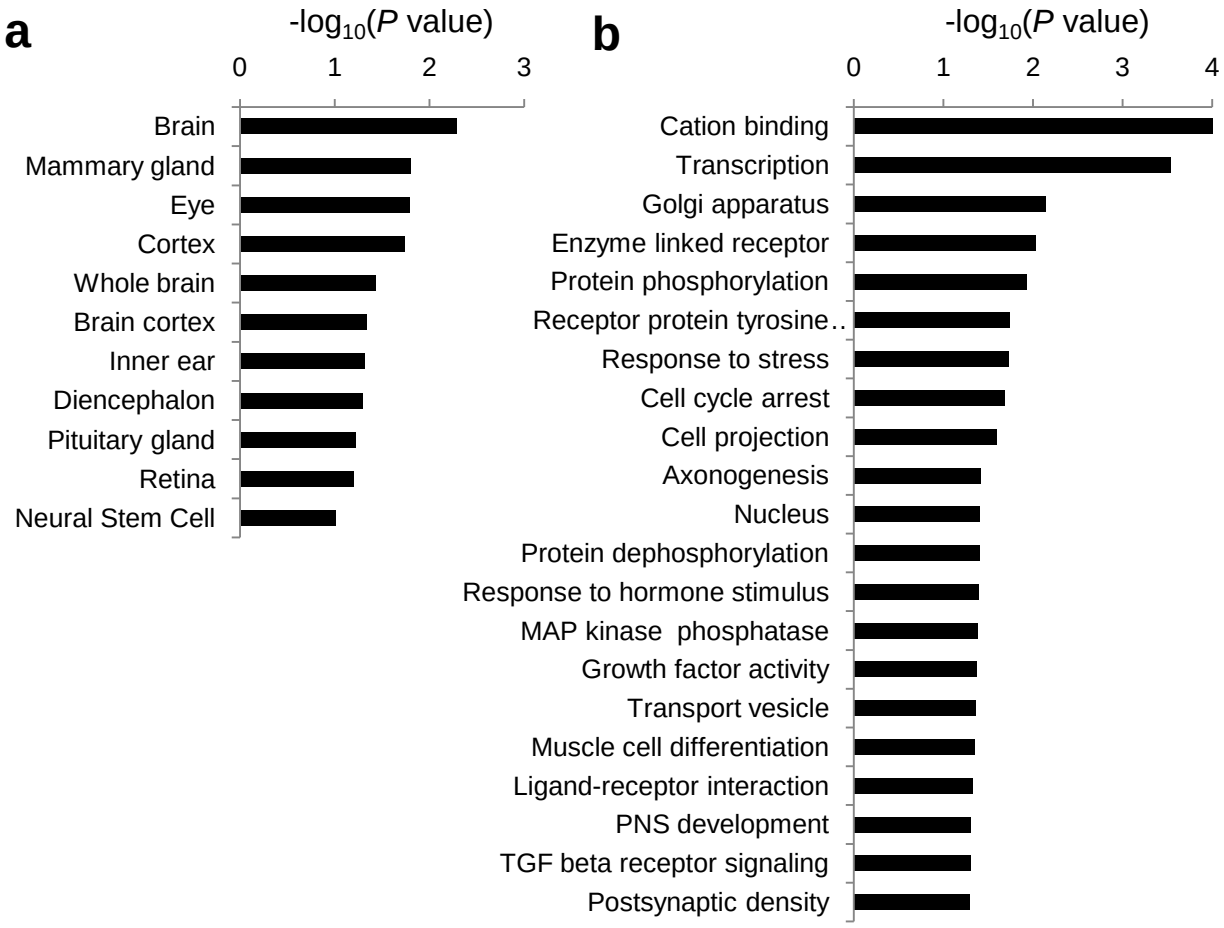

Supplementary Figure 20. Functional annotation of differentially expressed genes. Log_{10}-transformed *P* values are shown for tissue expression enrichment (**a**) and functional pathway enrichment (**b**) of genes, which were differentially expressed in adult dentate granule cells *in vivo* between E0 and E4, and targeted by at least one MSCC30+ site.

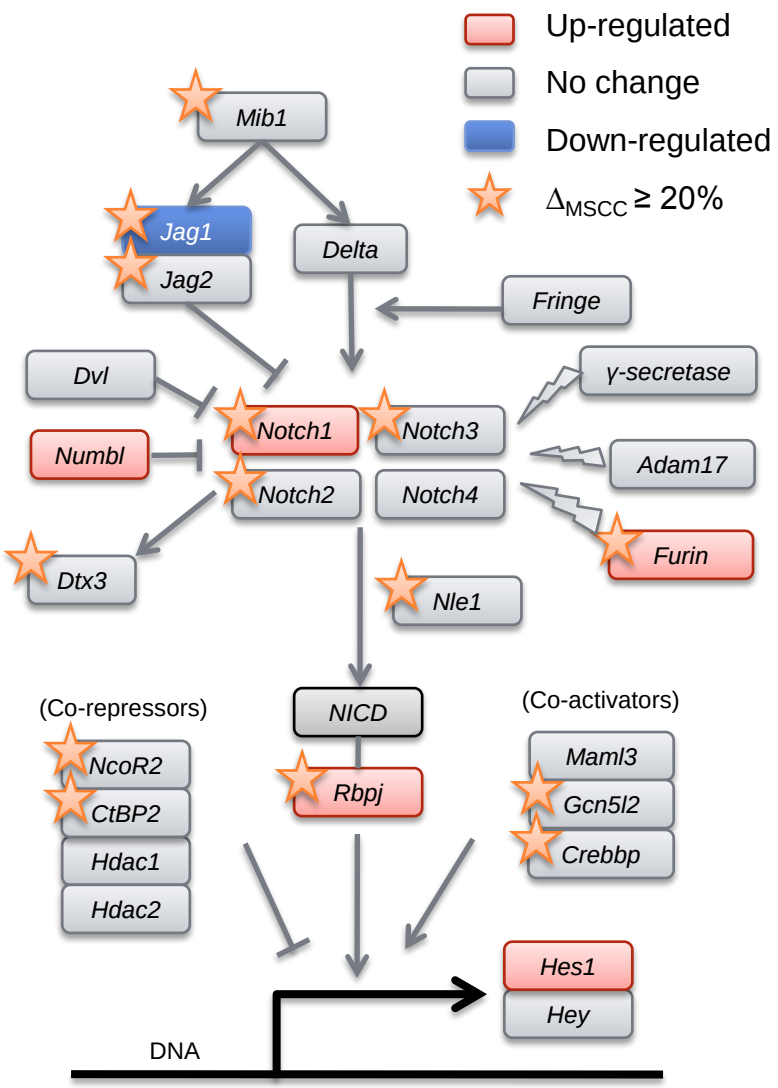

Supplementary Figure 21. Notch signalling pathway is a target of activity-induced CpG modification. Shown is a schematic diagram of Notch signalling pathway (modified from KEGG; www.genome.jp). Genes that harbour methylation changes are indicated by stars. Expression changes of individual genes are colour-coded.

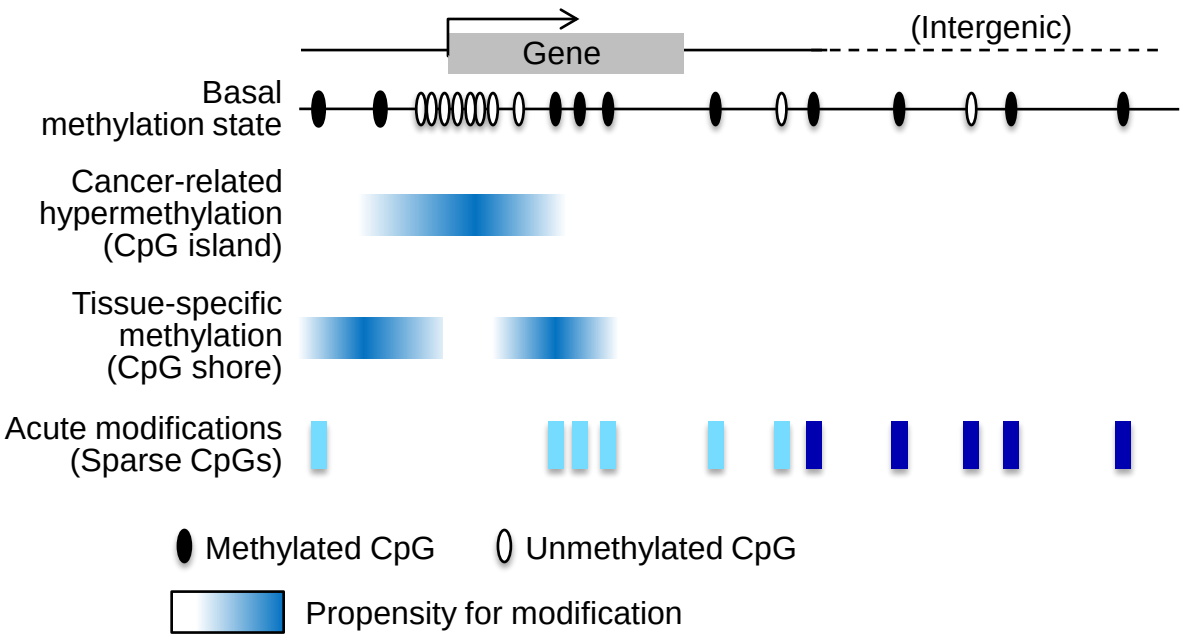

Supplementary Figure 22. A model on differential modulation of CpGs in specific genomic contexts in different biological processes. Highly clustered CpGs form CpG islands around TSSs of genes and are mostly unmethylated at the basal state. CpG-island-associated hypermethylation often occurs at tumor suppressor gene promoters in cancer (ref[46]). Recent studies have also identified a subset of CpGs located near CpG islands that are subjected to tissue-specific and/or cancer-related methylation (CpG shores; ref[45]). Sparse CpGs outside CpG islands are preferential targets for stimulus-dependent acute modifications in fully differentiated cells *in vivo*, including both gene bodies and intergenic regions.